Review Article

Parallel-plate avalanche counters for heavy-ion beam tracking: History and mysteries

Salvatore Di Carlo* and Marco Cortesi

Facility for Rare Isotope Beam, Michigan State University, East Lansing, Michigan, USA

(Received 3 November 2023; accepted 29 March 2024; published 25 April 2024)

Despite being an old detector concept, position-sensitive parallel-plate avalanche counters (PPACs) remain widely used today for heavy-ion position and timing measurements. In modern rare isotope beam facilities and large-acceptance fragment separators, PPACs are used to characterize beam properties (diagnostics), facilitate beam delivery (tuning), and provide event-by-event beam tracking for particle identification (PID). Most popular particle localization methods in PPAC detectors are based on strip electrodes electrically connected to resistive-chain circuits or delay lines. More exotic systems include optical readouts based on recording electroluminescence light with high-granularity photodetector arrays or high-resolution resistive anode electrodes. PPACs with conventional resistive-chain or delay-line readouts achieve typical position and time resolutions of below 1 mm (σ) and around 150 ps (σ), respectively. In addition, delay-line systems are capable of counting rates above several hundred kHz for beam areas of a few millimeters square, and around 1 MHz for larger beam sizes. Resistive-chain readouts have limited rates of a few tens of kHz. A review of the operation principles and performance of PPAC detectors is presented in this paper. We will discuss decades-long experience building and operating PPACs developed at the National Superconducting Cyclotron Laboratory, and then refined at the Facility for Rare Isotope Beams (FRIB), mostly focusing on the delay-line readout technique (DLPPAC). We will also discuss problems that arise due to electric discharges at high rates and briefly describe ongoing developments at FRIB.

DOI: 10.1103/PhysRevAccelBeams.27.044801

I. INTRODUCTION

The parallel plate avalanche counter (PPAC) is an old gaseous detector concept originally introduced in 1952 [1], with the scope of detecting minimum ionizing particles at high rates and measuring the radioactive lifetimes of exotic decays. The implementation of PPACs rapidly expanded into other fields in the following years [2–4].

PPACs are of simple construction, easy to maintain and service, and their operation does not require complex interfaces. However, in parallel-plate configurations, the electrodes are fully exposed to the large amount of photons and ions created during the avalanche process. This causes large photon- and ion-mediated secondary effects that allow only moderate gas gains. As a result, the use of PPACs is mainly restricted to the detection of highly ionizing radiation.

When operated at low pressure (typically <15 Torr), PPACs can be made of a small material budget ($<1\ \mathrm{mg/cm^2}$), which is essential for ensuring the minimization of energy loss and angular straggling, and avoiding the production of charge states of heavy-ion beams. Position-sensitive PPAC detectors operating at low pressure are still regarded today as the only practical solution for event-by-event heavy-ion tracking, so they are actively being developed and implemented in various beam accelerator facilities around the world. A few representative examples include beam diagnostics at REX-ISOLDE [5] and n_TOF [6] facilities at CERN, particle identification (PID) for the focal plane detector system of the BigRIPS fragment separator at RIKEN [7], and beam monitoring under development for the planned KOrea Broad acceptance Recoil spectrometer and Apparatus (KOBRA) in South Korea [8]. This present manuscript provides an overview of PPAC operating principles, discusses the main properties and performance of different readout configurations, and describes technologies, materials, and techniques currently available for the fabrication of the major detector components. To conclude, we will provide a general overview of the delay-line PPAC detectors that are currently used at the Facility for Rare Isotope Beams (FRIB) to diagnose beams at the Advanced Rare Isotope Separator (ARIS) and in other beam lines. The present detector design is the result of several decades of

*dicarlo@frib.msu.edu

experience in fabricating, developing, maintaining, and operating beam diagnostic devices, started at the National Superconductive Cyclotron Laboratory (NSCL) [9] and then refined at FRIB.

II. OPERATIONAL PRINCIPLE

Among all radiation detection configurations, the gas avalanche parallel-plate geometry is the simplest and most straightforward. It consists of a small gap, typically 3–4 mm wide, sandwiched between two flat electrodes maintained at different potentials and filled with a suitable gas mixture. Under these conditions, a uniform electric field is established across the gas gap. Electrons and ions, released within the detector volume by ionizing radiation, drift toward the respective electrodes under the influence of the electric field; the electrons toward the anode and the ions in the opposite direction. For very large reduced electric field intensities (>300 V/cm/Torr), electrons are accelerated at energies large enough to create secondary electrons via ionization processes, in the so-called electron avalanche mode. As a result of the motion of positive and negative charges in the gas gap, electrical signals of equal intensity, but opposite polarity, are measured on the load coupled to the electrodes.

The intensity of the instantaneous current induced by moving charges $q(t)$, with velocity $\vec{v(t)}$, on a particular electrode A can be computed by applying the Shockley–Ramo theorem [10,11]:

$$i_A(t) = q(t)[\vec{E_w} \cdot \vec{v(t)}]. \quad (1)$$

$\vec{E_W}$ denotes the weighting field sensed by the measuring electrode: this is the field that would prevail at a given instantaneous charge position q with all electrodes grounded, except for the sensing electrode set to unit potential (1 V). For a parallel-plate configuration, the weighing field is uniform with a strength proportional to $1/d$, where d is the distance between the anode and cathode electrodes. By applying the Shockley–Ramo theorem and assuming that the distribution of the initial electron-ion pairs released in the PPAC is uniform and extends along the entire gas gap, the current induced on the anode by the avalanche electrons as a function of time can be calculated as [12]:

$$i_e(t) = -\frac{en_0}{T_e} e^{\alpha v_e t}\left(1 - \frac{t}{T_e}\right) \qquad 0 \le t \le T_e, \quad (2)$$

where e is the elementary charge, n_0 is the total number of primary electron-ions pairs uniformly released in the gas gap, $T_e = d/v_e$ is the total collection time for the avalanche electrons (for a few mm gas gap T_e is of the order of few tens of nsec), α is the first Townsend coefficient of the filling gas (namely it expresses the number of secondary electron-ion pairs generated per unit length), and v_e is the electron drift velocity.

Based on similar arguments, an expression for the components of the signal induced by avalanche ions $i_i(t)$ can be derived. However, for the ions, there are two distinct components (Fig. 1, left side): the first one appears as soon as the primary electrons are released ($t = 0$), and it ends when all the electrons are collected at the anode ($t = T_e$). In this phase, as the avalanche develops, ions are progressively generated along the gas gap. The second component occurs when all the electrons have been collected at the anode ($t = T_e$), and the ions are the only charges left in motion in the gas gap; in this stage, there is no further creation of electron-ion pairs. Once all the charges have been collected and neutralized at the respective electrodes ($t = T_e + T_i$), the induced currents cease. As ions are generally 100–1000 times slower than electrons in gas ($v_i \ll v_e$), their collection time T_i is considerably longer (a few microseconds) than that of

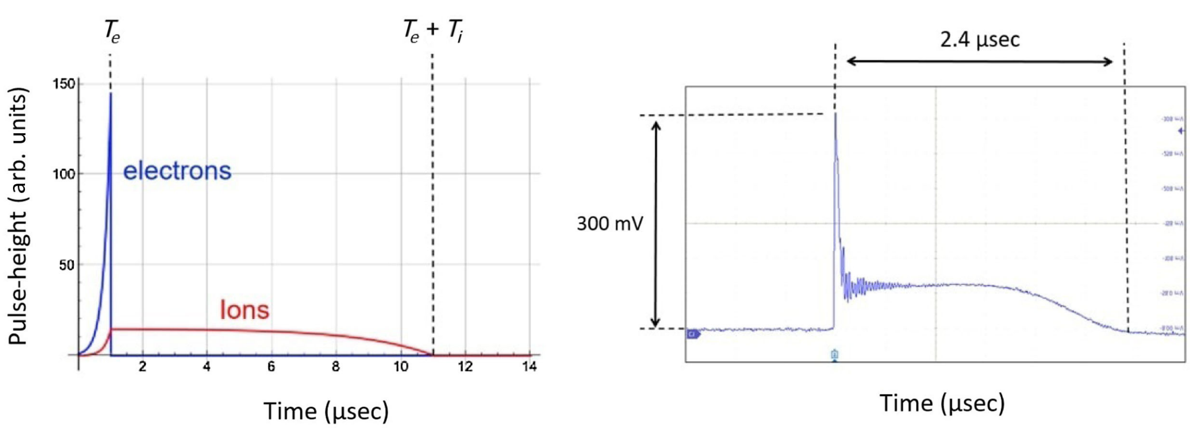

FIG. 1. Comparison of calculated (left) and measured (right) signals induced on the PPAC anode electrode. The snapshot depicted on the right panel was obtained by irradiating a PPAC with 5.9 MeV α-particles from an Am-241 source. The PPAC (3.5 mm wide) was operated in isobutane at 7 Torr and the signal was processed by a fast-current preamplifier.

electrons T_e (a few tens of nanoseconds), and the current induced by ions can be simplified as follows [12]:

$$i_i^{(1)}(t) = -\frac{en_0}{\alpha d T_i}(e^{\alpha v_e t} - e^{\alpha v_i t}) \qquad 0 \le t \le T_e, \tag{3}$$

$$i_i^{(2)}(t) = -\frac{en_0}{\alpha d T_i}(e^{\alpha d} - e^{\alpha v_i t}) \qquad T_e \le t \le T_e + T_i. \tag{4}$$

The right side of Fig. 1 shows an oscilloscope snapshot of a typical fast signal recorded at the cathode electrode of a PPAC. The signal was recorded with the detector filled with isobutane at 7 Torr and irradiated by α particles emitted by an Am-241 source. With the exception of a much longer ion tail, which depends upon the ion mobility assumptions made in the model, the analytical reconstruction of the induced signal, corresponding to the sum of the three components defined by Eqs. (2)–(4), is a fairly accurate representation of the measured signal. Nevertheless, it should be noted that a current signal measured on the load of an electrode is actually the result of convolution between the actual measured current and the response function of the preamplifier used to process the pulse, so the observed response may be slower than predicted.

Upon collection of all negative and positive avalanche charges at the respective electrodes, the total, integrated charge induced on a given electrode equals the amount of charge collected on this electrode. For instance, the total charge induced on the anode by the avalanche electrons (q_e) and ions (q_i) can be computed, respectively, as

$$q_e = \int_0^{T_e} i_e(t)\,dt = -\frac{en_0}{\alpha^2 d^2}(e^{\alpha d} - 1) \approx -\frac{en_0}{\alpha^2 d^2} e^{\alpha d}, \tag{5}$$

$$\begin{aligned} q_i &= \int_0^{T_e} i_i^{(1)}(t)dt + \int_{T_e}^{T_i} i_i^{(2)}(t)dt \\ &\approx \int_0^{T_i} i_i^{(2)}(t)dt = -\frac{en_0}{\alpha d} e^{\alpha d} + \frac{en_0}{\alpha^2 d^2}(e^{\alpha d} - 1). \end{aligned} \tag{6}$$

The contribution of the first ion component $i_i^{(1)}(t)$ to the total induced charge has been neglected because the ions are basically stationary in the rest frame of the electrons ($T_e \ll T_i$).

The total integrated charge induced by the avalanche, as the results of the motion of the avalanche electrons and ions in the PPAC gas gap, under the action of a uniform electric field, is then equal to

$$q_e + q_i = -\frac{en_0}{\alpha d} e^{\alpha d}. \tag{7}$$

Similar results could have been obtained from the Townsend avalanche equation, considering the uniform distribution of primaries along the PPAC gas gap.

It should be noted that since the primary electrons deposited far away from the anode have paths in the gas much longer than their mean free path, they are more likely to undergo many ionization processes. In contrast, primary electrons created near the anode are likely to be collected without initiating multiplications. Further, since the number of secondary electrons generated increases exponentially as the avalanche moves toward the anode, the majority of them are collected and neutralized within a short period of time. In essence, the avalanche occurs only in a confined volume close to the anode, and thus only a fraction of the primaries contribute effectively to the gas avalanche. This is quite a different scenario from the case where all the primary electrons are created at a single point near the cathode so that all the primaries equally contribute to the avalanche development, resulting in the integrated charge expressed as [13–15]:

$$q^* = -en_0\, e^{\alpha d}. \tag{8}$$

As a result, in PPAC detectors, and in general in configurations where the primary charges are distributed over a large volume within the avalanche region, the total integrated charge induced on the readout electrode is diminished by a significant geometrical factor. A comparison of Eqs. (7) and (8) reveals that only $(1/\alpha d)$ of the total primary electrons deposited in the PPAC gas gap are contributing to the avalanche. For a typical 3 mm wide gas gap, at gas gain approaching 10^4, PPAC's sensitivity to the energy deposited by the impinging particle is reduced to just 10%. The low energy resolution provided by PPAC detectors is mainly caused by the low sensitivity to the primary deposited in the gas gap and the wide statistical variance of the avalanche process.

A thin metallic mesh (Frisch grid) can be used to separate the drift region from the avalanche volume in order to restore the full sensitivity to the primary electrons deposited in the parallel-plate gas gap (see, for instance, figure 7.18 in [16]). High electron transparency across the mesh is achieved when the avalanche field is several times larger than the field across the drift region, a condition that is generally achieved under normal operation at moderate gain. The same principle is used in modern Micro-Mesh Gaseous Structure (MicroMegas) [17]. Nonetheless, this solution is not suitable for heavy ion tracking applications because the mesh wires will absorb a significant portion of the beam particles, reducing significantly the detection efficiency.

Furthermore, compared to the ion component, electrons contribute with a small fraction to the total induced charge: under normal operating conditions (namely $7 \le (\alpha d) \le 10$), the q_e to q_i ratio is only a few percent [see Eqs. (5) and (6)]. Accordingly, readouts based on integrated charges, where both electrons and ions make up for the output signal, have a much higher sensitivity than readouts based only on fast avalanche electron signal, at the expense of a much lower counting rate capability.

A. Timing measurement

Timing measurements are performed by processing the rise time of the fast signals induced by the avalanche electrons. Rise time is defined as the length of time required for a signal to increase from 10% to 90% of its maximum value (Fig. 2). A detailed calculation of the PPAC signal rise time can be computed analytically. The interval of time at which the current i_e reaches its maximum value can be calculated from Eq. (2):

$$t_{\max} = T_e\left(1 - \frac{1}{\alpha d}\right) \tag{9}$$

and the maximum value of the induced current at $t_{\max}$ equals to

$$i_{\max} = -\frac{en_0}{\alpha d T_e} e^{\alpha d - 1}. \tag{10}$$

Combining Eqs. (2) and (10), we can determine the time t_f at which a certain fraction (f) of maximum induced current $i_{\max}$ is reached on the signal, namely,

$$f = \frac{i_{(t_f)}}{i_{\max}} = \alpha d e^{\alpha(v_e t_f - d)+1}\left(1 - \frac{t_f}{T_e}\right)$$
$$\Rightarrow t_f = T_e + \frac{W_{-1}(-\frac{f}{2.71828\ldots})}{\alpha v_e}, \tag{11}$$

where $W_{-1}(\mathrm{x})$ is the second value of the Lambert W function, solution of the equation $f = x \cdot \exp(x)$ for $-1/e < x < 0$ [18], and $e^1 = 2.71828\ldots$ is the Euler's

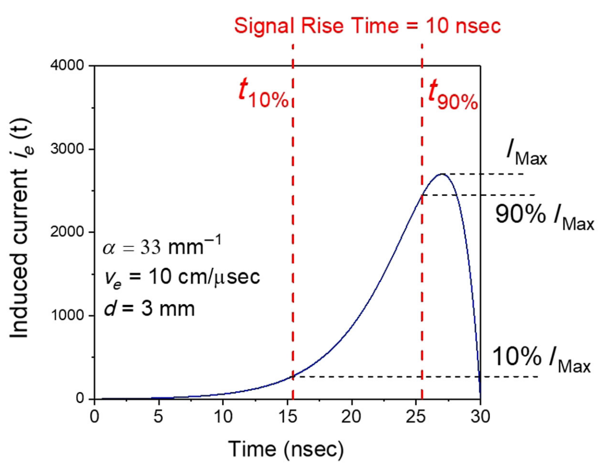

FIG. 2. Fast electric current profile induced on the anode by electrons moving across a 3 mm thick PPAC, computed according to Eq. (2). Parameters used for the calculation are given in the figure.

number. To avoid confusion with the symbol of the elementary charge (e) at the beginning of Sec. II, we have explicitly written the value of Euler's number ($e^1 = 2.71828\ldots$) instead of its symbol. The rise time is thus computed as

$$T_{90\%-10\%} = t_{90\%} - t_{10\%}$$
$$= \frac{W(-\frac{0.9}{2.71828\ldots}) - W(-\frac{0.1}{2.71828\ldots})}{\alpha v_e} \approx \frac{3.36}{\alpha v_e}. \tag{12}$$

It is particularly noteworthy to observe that for detectors with an extended and uniform distribution of primary electrons, the rise time of induced signals does not depend on the size of the gas gap (d), but only on the size of the avalanche (through the first Townsend coefficient α) and the drift velocity v_e. At very high reduced fields, we can also make use of the approximation $\alpha \approx 1/\lambda_m$, where λ_m is the electron mean free path [19]. This is a consequence of the fact that the first Townsend coefficient at high reduced electric fields depends almost entirely on the mean free path of the electrons. Thus we can also write

$$T_{90\%-10\%} \simeq 3.36 t_{\lambda_e}, \tag{13}$$

where $t_{\lambda_e} = \lambda_e/v_e$ represents the average time between two consecutive collisions of an electron with a gas molecule. The quantity t_{λ_e} is a function of different parameters, including the electric field strength, the type of gas, and the pressure. For a typical amplification gap of 3 mm, an avalanche drift velocity of 10 cm/μsec, and a first Townsend coefficient α equal to 333 cm^{-1}, the rise time of the induced signal would result in about 10 nsec, which is a typical value measured in low-pressure PPAC detectors, filled with pure quenching gases (e.g., isobutane), in normal operational conditions.

The short rise time of PPAC signals can be explained by the exponential nature of the multiplication process. As the electron cloud moves through the gas, the avalanche signal increases exponentially and the corresponding signal cannot be detected until the electron cloud reaches the very last portion of the gas gap between the electrodes (a few hundreds of micrometers). The short fall time is rather associated with the longitudinal extension of the avalanche electron distribution.

As a result of the above arguments, it is evident that the time resolution of a PPAC detector, as a measure of the dispersion of its time response, can be affected by a variety of factors, including statistical fluctuations in gas gain; variations in the electric field, such as resulting from an irregular gas gap which affects the strength of the electric field locally; and finally an uneven, sparse deposition of primary electrons within the gas, which may occur, for instance, with extremely light particles and low-pressure

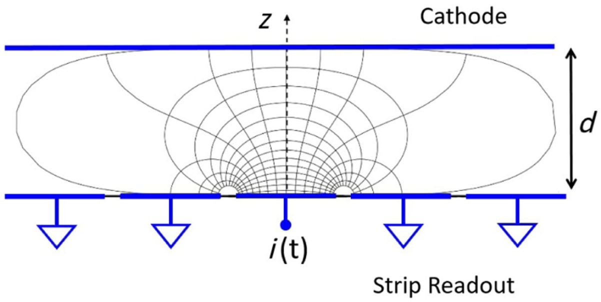

FIG. 3. Graphical representation of the weighting field lines computed for the central strip of a segmented anode.

gas, as a consequence of low energy deposited in the detector volume.

The unique features of low-pressure PPACs applied to heavy-ion physics, such as a short rise time, their simple construction that allows for homogeneous gas gaps, the dense and uniform distribution of primary ions released into the gas gap, and the good stability reached even at large avalanche sizes, allow this detector technology to achieve excellent time resolution (<150 psec σ). This result is comparable to that reached by conventional plastic scintillators read by vacuum photomultiplier tubes, routinely used for time-of-flight measurements.

B. Signals induced on a segmented anode foil

The processing of signals induced on a segmented anode can be used for encoding the particle localization. However, the computation of avalanche-electron-induced signals on a segmented strip anode via the Shockley-Ramo theorem is more tedious and cumbersome, with a weighting field that assumes a complex structure (Fig. 3).

On the other hand, some significant considerations can still be derived from a simple model if some general assumptions are made. We assume that a primary ionization electron of charge q is generated in a single event at some distance z from the readout strip, at the time $t = 0$. The electrons are free to move toward the segmented anode under a uniform electric field, but no amplification will occur. This electrode is segmented into strips of width w in one direction and infinitely long in the other direction. We also assume that the charges are located on top of the central strip, from which the signals are read out—see Fig. 4.

By using the method of image charges, it is possible to calculate the density of the charge induced on the strip by the electrons with charge q, as a function of the distance from the readout strip. As the electrons move toward the anode at a constant velocity v_e, the density of induced charge on the strip varies according to Eq. (14), causing electric current to flow into the strip [see Eq. (15)] [20].

$$q_{\text{strip}}(z) = \frac{2q}{\pi}\tan^{-1}\left(\frac{w}{2z}\right), \tag{14}$$

$$\begin{aligned} i_{\text{strip}}(t) &= -\frac{dq_{\text{strip}(z)}}{dt} = -\frac{dq_{\text{strip}(z)}}{dz}\frac{dz}{dt} \\ &= \frac{4qwv_e}{\pi(4z^2(t)+w^2)}. \end{aligned} \tag{15}$$

In accordance with Eq. (14), the total induced charge on the readout strip increases sharply with decreasing electron distance from the anode z. Additionally, at any distance z, the induced current increases as the strip width w decreases [Eq. (15)]. It can be easily calculated that 50% of the total induced charge sensed by the strip is achieved when the

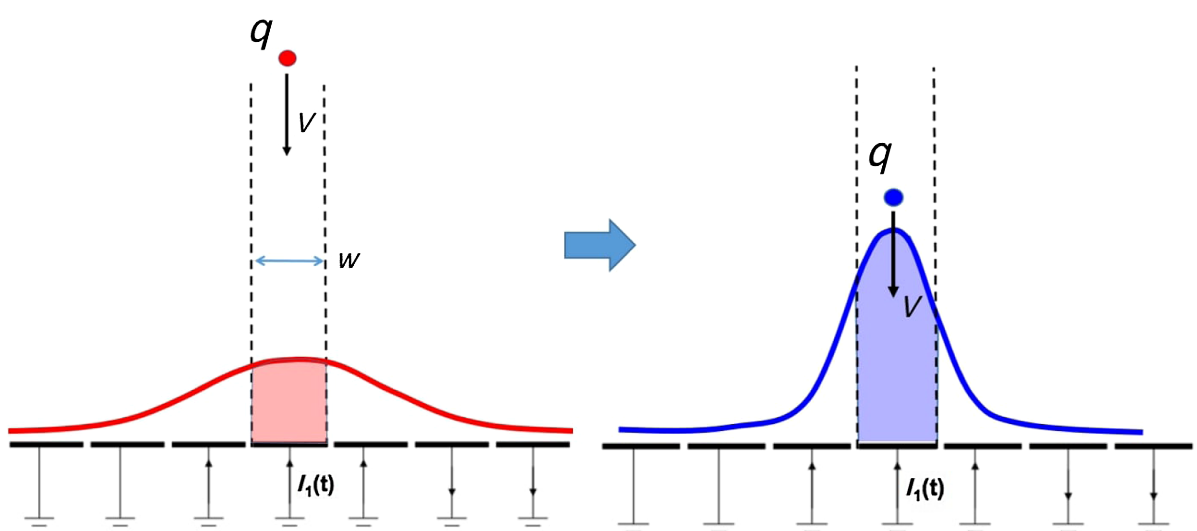

FIG. 4. Illustrations of different charge densities induced by a charge (q) located at different distances from a segmented anode. For each position, the area under the distributions corresponds to the total charge accumulated in the central strip. When the charge (q) moves from one position to another, a current is induced to compensate for the variation in the integral charge accumulated on the strip.

electrons are collected on the strip from a distance equal to half of the strip width, namely

$$q_{\mathrm{strip}}\left(\frac{w}{2}\right) = 0.5q. \tag{16}$$

Strips with a width of a few tens of micrometers show a spike in the induced current in correspondence with the electrons approaching the readout, which is very similar to pure charge collection mechanisms. This is also the case with multiwire proportional counters, designed with small diameter wires so that gas avalanche processes occur basically on the very surface of the wires and are capable of fast charge collection with a time resolution of a few tens of psec [21]. However, because of the long tail of the signal induced on the wire by the electrons that move in a highly in-homogeneous field (the field strength varies like $1/r$ where r is the distance from the wire), there is a significant ballistic deficit which results also in a low sensitivity: similar to the PPAC, only a fraction of the avalanche electrons contribute to the induced signal when the primary electrons are deposited over a large volume within the avalanche region.

For the reason discussed above, very narrow conductive strips are desirable, both in terms of spatial and time resolutions. Despite this, there are severe challenges in fabricating PPACs that are required to be used as a position-sensitive detector for heavy-ion tracking. The electrodes of low-pressure PPACs, fabricated at a low material budget for minimal straggling, are generally made of very thin polymers on which metal layers are deposited by thermal evaporation or sputtering. Anode strips are commonly fabricated using dedicated masks capable of reaching down to a mm size at an acceptable tolerance.

III. TOWNSEND DISCHARGE IN PPAC

The purpose of this section is to review the main mechanisms, outcomes, and phenomena related to discharge formation in parallel-plate detector configurations. As with all gaseous detectors, electron avalanche multiplication cannot be increased arbitrarily in PPACs. There are several types of problems that can limit gas gain and lead to electric discharges. The most trivial causes of instabilities are mechanical imperfections in “bad” detectors, including sharp edges at high potentials leading to Corona discharges or spontaneous electron emission, or dust and other conductive materials left from the production process in between the electrodes. Generally, discharges due to imperfections are well localized and persist under well-defined conditions, so they are easily identified and corrected. In reliable “good” detectors, we can distinguish two more mechanisms that lead to instabilities, denoted as slow and fast breakdown [22].

A. Slow breakdown

Slow breakdown may appear in gaseous detectors operated in proportional mode because of an intense photon or ion feedback. The photon feedback occurs because of the large amount of light emitted by the avalanches that generate photoelectrons from the photosensitive elements in the chamber, either the metallic electrodes or the gas itself. These photoelectrons induce secondary avalanches following the initial one [23]. Similarly, positive ions that slowly move toward the cathode may, through impact on the electrode surface, extract electrons and cause secondary avalanches, in the so-called ion-feedback process [24]. In both cases, the generation of a secondary-avalanche feedback leads to a fast transaction from proportional mode to streamer and thus to electric discharges. When feedback-generated secondary avalanches contribute significantly to the signal, there may be several undesirable effects, including loss of position resolution and counting rate. Further, the accumulation of successive secondary avalanches in a continuous feedback process, potentially divergent, might make the amplification unstable and limit the maximum achievable gas gain. Typical breakdown development time ranges from a few μsec to a msec, depending on the gas type, detector geometry (gas gap), and the nature of the feedback that triggers the discharges: photon-mediated discharges are faster than those caused by ion feedback. The general condition for a stable operation is achieved when

$$G\gamma_{\mathrm{ph}} < 1 \tag{17}$$

and

$$G\gamma_{+} < 1, \tag{18}$$

where G is the gas gain, and γ_{ph} and γ_{+} are the probability of creating a secondary electron due to the photoionization of the gas and ion recombination on the cathode, respectively.

In gaseous detectors, photon feedback generally dominates ion feedback, especially in detectors with an open geometry configuration, such as PPACs, in which electrodes are fully exposed to avalanche emissions. Nevertheless, slow breakdowns are generally not a problem for detector stability, except in the presence of extremely photosensitive surfaces or in the absence of a well-quenched gas mixture. For operations at low pressure needed for heavy-ion tracking, because of the rarefied filling gas, the quenching mechanism of avalanche photons is extremely inefficient. Therefore, slow breakdowns are one of the major causes of discharge in low-pressure PPACs, unless the detector is filled with a pure quenching gas (for example, with alkane gases, such as isobutane).

B. Fast breakdown

In the absence of feedback effects, a different mode of breakdown occurs, known as fast breakdown [25]. It is characterized by an initial avalanche followed by a spark after a few tens of nanoseconds. The fast breakdown occurs after an intense space-charge-induced distortion of the electric field, occurring in the proximity of the avalanche, as a consequence of an extremely high gas gain. Furthermore, high gains also cause intense short-distance photoionization of the gas molecules. The rapid generation of photoelectrons, drawn toward the avalanche under the action of the distorted field, contributes to a rapid propagation of the avalanche size over larger volumes. The accelerated growth of multiplying charges is more pronounced at the front and back of the avalanche, where the electric field is stronger. The result is the formation of a conductive filament of fully ionized gas (streamer) that spreads across the entire gas gap. This closes the space between the electrodes, triggering the spark breakdown. A schematic representation of the process of fast breakdown is shown in Fig. 5.

It was empirically found [12] that the start of the condition for the transition from proportional mode to streamer due to the fast breakdown mechanism is met when the total charge in the avalanche reaches 10^8 electrons (Raether criterion), namely

$$Gn_0 > 10^8, \tag{19}$$

where G is the gas gain and n_0 is the number of primary electrons.

A similar condition for the onset of the streamer is when the space-charge field induced by the avalanche reaches a comparable level to the external electric field (Meek's criterion) [27].

There is a widespread experimental consensus that the limit for streamer formation is independent of gas gain (G) since it depends only on the total charge of the avalanche. Unlike the slow breakdown mechanism, the limit for fast breakdown discharges does not depend on the composition

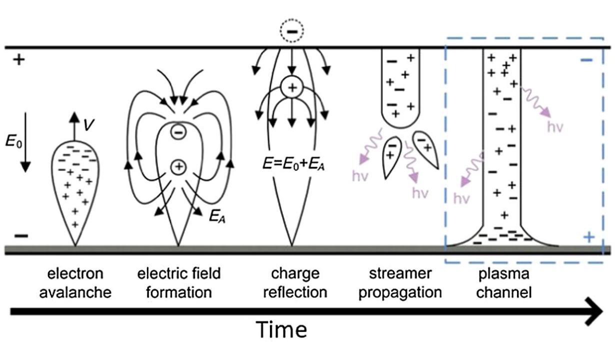

FIG. 5. Schematic representation of the transition from proportional avalanche mode to streamer due to the fast breakdown mechanism. Figure taken from Ref. [26].

of the gas. However, due to fluctuations in the avalanche statistic and variations in the number of primaries deposited by the incident ionizing radiation, the Raether limit is never strictly met in practice. The maximum number of avalanche charges in "real" detectors reach values of about 10^6–10^7 electrons, assuming the case of pointlike concentration of primaries, and a little higher for extended tracks.

In the case of low-pressure PPACs for heavy ion physics, where many ion species are present simultaneously, the maximum achievable gain is imposed by the most ionizing beam particle (with the highest atomic number Z). This limits the dynamic range of the device, particularly when it is necessary to track the full spectrum of ions traveling along the beam line. The range of energy loss covered by a low-pressure PPAC detector using fast signal readouts is quite modest (approximately just above 1 order of magnitude in energy), while charge integration readout systems achieve a much greater dynamic range (estimated at over 2 orders of magnitude).

C. Breakdown induced by high beam rate

It has been experimentally observed that there is a systematic rate-dependent reduction of the maximum achievable gains as a consequence of the accumulation of charges from the merging of consecutive avalanches [16,20,28]. As shown in Fig. 6, the maximum achievable gain rapidly decreases when the rate exceeds 10^2–10^3 Hz mm^{-2}, a characteristic that is common to a variety of gaseous avalanche detectors. A simplified explanation of the

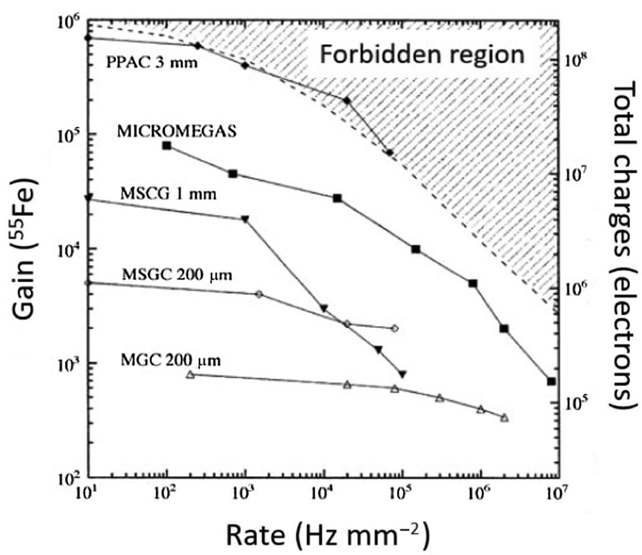

FIG. 6. Relation between the total avalanche charge and the irradiation density (rate), for different gaseous detector technology. The forbidden zone is dominated by fast breakdown mechanisms (spark discharge). The allowed zone is the region of operation of gas detectors without a spark discharge, featuring a progressive reduction of the maximum as a function of the rate. Figure taken from Ref. [29].

phenomena can be given based on a statistical argument. Positive ions left behind in the avalanche volume travel much slower than electrons collected rapidly on the anode. For example, in PPAC detectors of around a 3 mm thick gas gap, several microseconds are required for most ions to reach the cathode, where they are collected and neutralized. A two-avalanche sequence occurring at the same location will cause the second avalanche to be exposed to the ions left over from the first avalanche. It is possible that the progressive accumulation of charges could lead to a space-charge field comparable to that of the applied external field, which would affect the multiplication process and therefore reduce the effective gas gain.

Furthermore, if the field distortion is sufficiently high, the enhanced electron multiplication in the front part of the second avalanche may exceed the threshold for triggering a fast breakdown. If some degree of gas self-photoionization is also present, amplification of those photoelectrons through the rear part of the avalanche will generate a cathode-directed streamer. A higher counting rate increases the likelihood of overlapped avalanches.

For heavy-ion tracking purposes, the required low density of the gaseous media limits the detector performances in terms of stability, from effects arising from both photon-mediated feedback and rate-induced space-charge instabilities. Given a rate limit of 10^3 Hz mm^{-1} imposed by space-charge effects on the gas gain and assuming a small beam spot, for instance, in proximity to a beam focal point, with diameter of about 10 mm, PPAC may achieve spark-free operations with full detection efficiency only at maximum rates of around 100 kHz. In the case of dispersed beams, higher rates (>1 MHz) can be achieved with lower probabilities of rate-induced discharges, with the only rate limitation being the performance of the position-sensitive readout technique, as well as of the related electronics.

IV. MECHANICAL DESIGN

A typical two-dimensional (x, y) PPAC consists of a couple of position-sensitive parallel-plate counters, one for each coordinate. Each counter is made up of a 3–4 mm wide gas gap sandwiched between two thin conductive electrodes: a segmented (strip) anode and a uniform cathode that is common to both counters. A schematic design of a two-dimensional position-sensitive DLPPAC is provided in Fig. 7. Popular materials used for the electrode substrate include polypropylene [9], polyester [7], and mylar [8,30,31]. Polypropylene is widely used due to its low density (between 0.895 and 0.93 g/cm^3) and its robust mechanical properties, which include high fatigue and heat resistance [32], allowing thin foils to be stretched to produce thicknesses of a few micrometers.

Thin metal layers are formed on the insulating substrate to create conductive electrodes. Elements such as gold, silver [8,30], or aluminum can be deposited by e-beam or thermal evaporation, with typical thicknesses down to a few

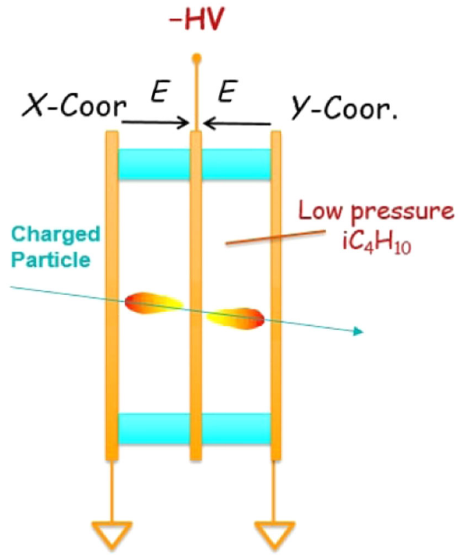

FIG. 7. Schematic design of a two-dimensional position-sensitive PPAC: A common cathode foil is sandwiched between two segmented anode electrodes. The latter, coupled with a suitable readout, provides the (X, Y) particles localization.

tens of nm [7–9,30,31]. To mitigate the disruptive effects of sporadic energetic discharges on the thin conductive surfaces, which may result, for example, in progressive degeneration of their electrical continuity, alternative materials such as chromium (which has a high melting point) or carbon (high electrical resistivity) can be considered.

Different techniques can be used for the deposition of the conductive coatings on the insulating substrates. In most cases, thermal or electron beam evaporation can be used to cover large surfaces up to several hundred nanometers in thickness. Photolithography is an alternative technique that has been successfully applied to the fabrication of PPAC electrodes [33]. Despite its high mechanical precision, this technique involves the use of thicker and more robust insulating substrates, resulting in some additional complications: for instance, thick electrodes lead to higher particle straggling and charge state production.

The electrode foils are typically fastened directly to a printed circuit board (PCB), which acts as a mechanical support and hosts the circuitry for the signal readout—see Fig. 14. The segmented electrodes that enable localization are most commonly fabricated by placing dedicated masks in front of the insulating substrates during evaporation. The level of segmentation of the cathode foils affects the detector's performance in terms of localization capability and time resolution. The most optimal granularity of the strip electrodes is dictated by the tolerance reached by the fabrication techniques for the mask and by the capability to align the electrode foils and the metal strip onto the supporting PCB boards. A striped electrode with a pitch of 1 mm and a length of up to 30 cm can be easily manufactured and can deliver a spatial resolution of 1 mm (σ) or below. The electrical contact between the electrode foils and the PCB's pads can be obtained by applying pressure to the foil with soft rubber bumpers or by using conductive cement.

As discussed in Sec. III A, when operating at low pressure, a pure quencher as a filling gas is required to suppress photon-mediated secondary effects, which becomes significant even at moderate gas gains. The alkane gases are a very good medium for PPACs: they show very similar working voltage ranges and a stable high-gain operation at low pressure. Examples of the most common gases used for PPACs include isooctane (C_8H_{18}) [9], isobutane (C_4H_{10}) [7,8,30,31,34], isobutylene (C_4H_8) [7], propane (C_3H_8), and n-butane [35]. All the aforementioned gases are easily available and inexpensive, but they pose safety concerns as they are highly flammable. Other nonflammable alternatives include greenhouse gases, but they are not easily at hand, for instance, hexafluoroethane (C_2F_6) [7] and octafluoropropane (C_3F_8) [7,8,30].

A metal vessel typically houses the inner electrodes mounted on PCB boards to reduce electronics noise and avoid contaminating the filling gas by outgassing. The vessel is additionally equipped with feedthroughs for both the anode HV bias and cathode readout signals, as well as suitable gas fittings for the interface to the gas handling system. As a transmission detector for heavy ion tracking, the vessel needs to be equipped with two thin pressure windows to seal the PPAC inner volume and allow beam transmission with minimal straggling. Pressure windows made of a few micrometers thick aluminized Mylar, or similar polymers, allow differential pressures of several tens of Torr, even in relatively large effective areas (up to about 500 cm^2).

V. READOUT METHODS FOR PARTICLE LOCALIZATION

Several readout methods can be employed to encode the particle localization in PPAC detectors. The more traditional approaches involve striped electrodes connected to charge-division circuits or delay lines (Fig. 8). More exotic, novel techniques, recently developed at FRIB, include pulse-height processing from signals sensed on the four corners of a uniform resistive plane and the recording of the secondary scintillation light using collimated arrays of photodetectors [e.g., Silicon-PhotoMultipliers (SiPMs)] [36]. This section is intended to provide a brief overview of the various readout technologies, including their main concepts, properties, and performance characteristics.

A. Charge-division method

In charge-division methods [9,37,38], particle localization is accomplished by connecting the cathode strips to a chain of resistors, with characteristic resistances of several kΩ/cm. Charge-sensitive preamplifiers process the signals and provide outputs proportional to the charge division between the two sections of the resistive chain (Fig. 8, left side). The charge-to-voltage outputs of the preamplifiers are fed into a Gaussian shaping linear amplifier and finally processed by an analog-to-digital converter (ADC) for spectroscopic analysis.

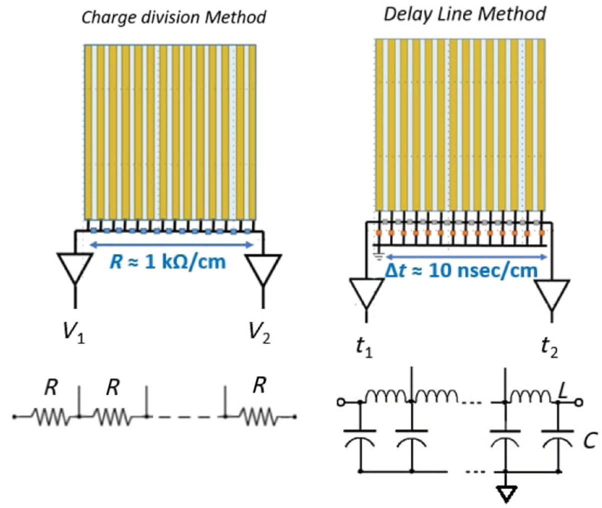

FIG. 8. Traditional localization encoding techniques used in low-pressure PPAC are based on charge-division circuitry (left) or delay line (right).

The position X and Y of the incident particle, which originally triggered the avalanche, is calculated from the outputs of the preamplifiers (Q_1^x, Q_2^x) and (Q_1^y, Q_2^y) as follows:

$$X = k_x \frac{Q_2^x}{Q_1^x + Q_2^x} + X_{\mathrm{offset}}, \tag{20}$$

$$Y = k_y \frac{Q_2^y}{Q_1^y + Q_2^y} + Y_{\mathrm{offset}}, \tag{21}$$

where the coefficients k_x and k_y are conversion factors (charge to distance), while X_{offset} and Y_{offset} account for parasitic resistances at the output that may result in a misalignment of the image center (0, 0).

Crosstalks between strips can lead to nonlinearity effects in the charge-ratio conversion, which in turn results in the spatial coordinates in the spectrum being a nonlinear function of the measured charges: this results in distortion of the final image. In order to reduce the effects of nonlinearity, it is imperative that preventive measures be taken when designing the geometry of a strip anode and avoid any possible parasitic impedance that may cause distortions.

It is worth noting that charge-sensitive preamplifiers operate at stable gain compared to other preamplifier designs, as the gain does not depend on the input capacitance or the amplifier bandwidth. In comparison with other readout techniques, the charge division method has a high signal-to-noise ratio, robust stability, and a wider dynamic range. However, the signal at the output of the charge-sensitive loop usually has a very long decay-time constant (up to a few microseconds), due to the need for a large feedback resistor to minimize its thermal noise contribution. This leads to limited rate capability as a consequence of a significant pulse pileup, with maximum rates reaching up to a few kHz. Submillimeter position resolution is achievable even at a relatively large area.

B. Delay-line method

The discrete-element delay-line readout is a common readout technique implemented in a variety of gaseous avalanche detectors (e.g., wire-based detectors [39–41], micropattern gaseous detectors [42,43]), as well as in vacuum devices (e.g., multichannel plate [44,45]).

In a typical delay-line scheme, the electrode strips are connected to discrete LC (inductor-capacitor) cells (Fig. 8, right side), which introduce a phase shift proportional to the number of elements crossed as the signal propagates through the circuit (Fig. 8, right side). The position is thus determined by comparing the time difference between signals at each end of the delay line:

$$X = k_x^t(t_1^x - t_2^x) + X_{\text{offset}}^t, \tag{22}$$

$$Y = k_y^t(t_1^y - t_2^y) + Y_{\text{offset}}^t, \tag{23}$$

where k_x^t and k_y^t are time-to-distance conversion factors, while X_{offset}^t and Y_{offset}^t recenter the image when affected by parasitic time delay in one of the outputs.

To extract the timing information from each output, the delay-line signals are processed by constant fraction discrimination (CFD) units, for analog-to-digital conversion, and then by a time-to-digital (TDC) converter. The latter outputs the time of arrival for each incoming pulse. The time stamps are obtained by processing the fast signals induced by the avalanche electrons while the slow ion component is ignored. The fast electron current is generally characterized by a typical rise time and width of a few nsec and a few tens of nsec, respectively. To reduce the possibility of recording random and uncorrelated events, an external trigger can be used to veto the TDC inputs. A timing filter amplifier can also be used to adjust the pulse shaping and improve the signal-to-noise ratio before CFD processing.

The design of delay-line circuitry needs to consider a bandwidth compatible with the detector operation range. Parameters to be determined are the number of cells in the line impedance and the values of the inductance (L) and the capacitance (C). Also crucial are the delay-to-rise ratio, which determines the density of the LC cells; the internal dc resistance of the inductors, which determines how attenuated pulses will be along the network; the total delay that imposed a constrain on the rate capability; and finally, the total delay-line impedance, which must match the input impedance of the load (the fast-current preamplifier) in order to minimize reflections due to transmission line effects.

As the contribution from the avalanche electrons is only a few percent compared to the total (electrons and ions) avalanche pulse, the pulse heights are smaller than the one obtained by the integrated charge method, resulting in a smaller dynamic range. However, the shorter pulse widths allow for high counting rate capability, only limited by the time length of the delay line, and by photon and ion feedback. Rate capabilities of up to 1 MHz can be attained at a detector efficiency close to 100%.

C. Uniform resistive-cathode foil

In place of a segmented conductive film, a uniform resistive cathode can be used to determine the localization of an event. The typical resistivity for the cathode electrode may range from a few k$\Omega/\square$ up to 1 M$\Omega/\square$. The uniform resistive electrode can be manufactured by evaporating a thin layer of resistive material, such as graphite, germanium, or diamondlike carbon on a typical thin insulator substrate.

The operational principle of this approach is based on collecting the induced charge, created during the avalanche process, on the resistive surface. Charges migrate toward terminals at the periphery of the resistive electrode in proportion to the resistance that those terminals perceive with respect to the position of the charges on the resistive surface. The avalanche localization, and thus the localization of the particle that triggered the avalanche, is accomplished by comparing the amount of charges collected at the terminals and implementing a localization algorithm that depends upon the readout geometry.

Examples of two different readout schemes are shown in Figs. 9 and 10. In the first configuration, signals are read out from the four corners of the cathode. In the second example, charges are collected from conductive strips that run along the four sides of the resistive electrodes. The reconstruction algorithms for extracting the position (X, Y) of the event in the two different cases are given in the figures. Images of a calibration mask recorded by irradiating the PPAC detector with 5.9 MeV α particles are also shown.

As evident from the analysis of the calibration images, the position resolution obtained provided by dissipative foil readouts is significantly superior to any method that uses segmented readouts. Position resolution of the order of tens of μm can be achieved on a relatively large surface. However, linearity distortions are a common problem for resistive anode techniques. The "four corners" readout is strongly affected by pincushion distortion, while the "four sides" readout exhibits barrel distortion along the margins of the image.

As a consequence of the extensive postprocessing necessary to correct distortions, as well as the poor rate

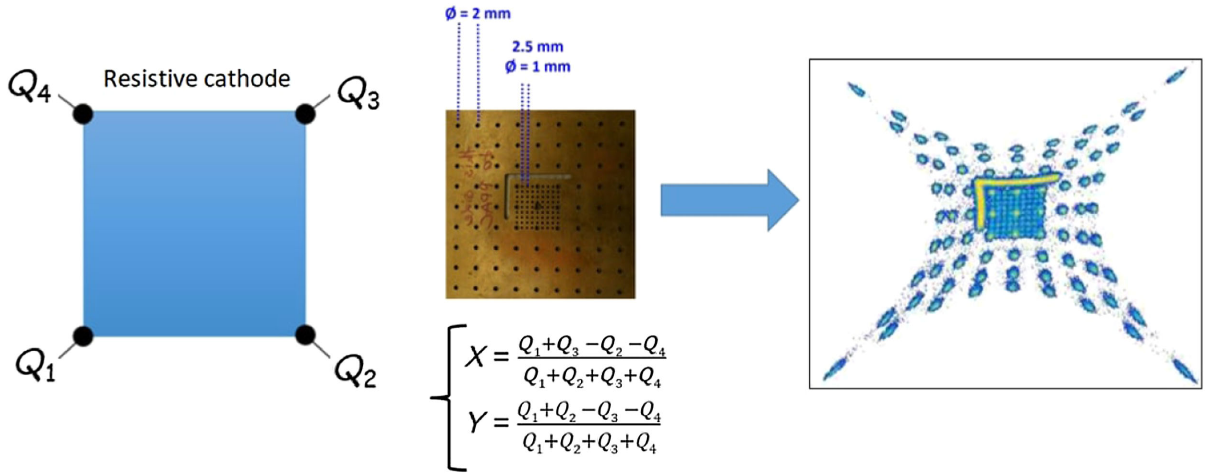

FIG. 9. Resistive foil technique with localization encoding processed by analyzing signals from the four corners of the cathode. The resulting image is affected by pincushion distortion.

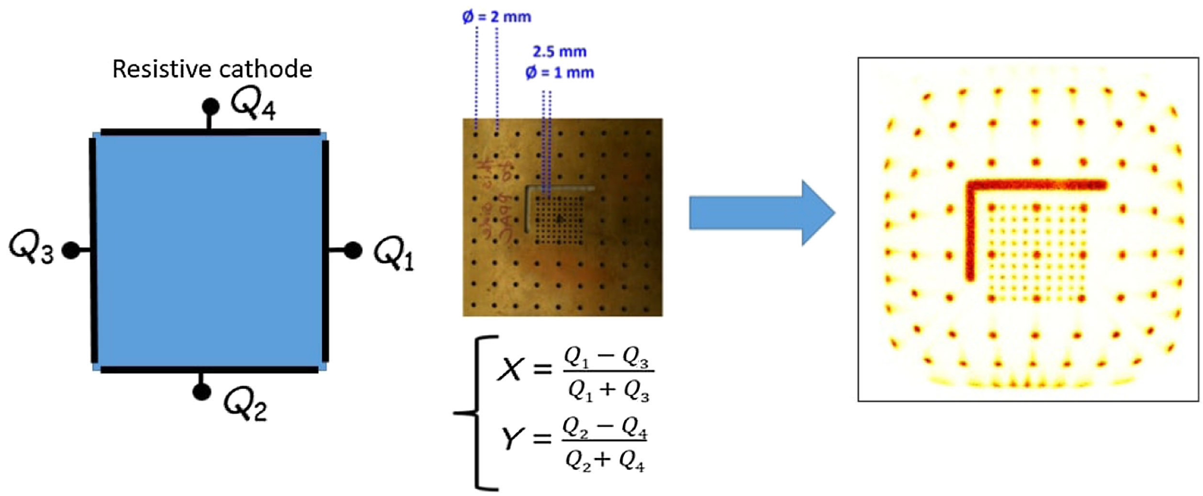

FIG. 10. Resistive foil technique with localization encoding processed by analyzing signals from the four sides of the cathode. The resulting image is affected by barrel distortion.

capability (up to a few kHz), uniform resistive cathode readouts have been less popular than delay line and resistive-chain configurations, even though they consist of a single counter and are therefore extremely simple to construct and extremely thin.

D. Optical readout

The electron avalanche process triggered by an ionizing event in gas not only multiplies charges by numerous sequential ionization processes but also produces scintillation light via secondary mechanisms (electroluminescence). Rather than relying on measuring avalanche charges, the large amount of scintillation light generated in a high-scintillation yield gas can be utilized for localization and obtaining timestamp measurements [46].

A simple design of a PPAC with an optical readout includes the following features: two parallel, thin electrode films, separated by a small gap (typically 3–4 mm), filled with low-pressure (<50 Torr) scintillating gas mixture; high granularity arrays of collimated photosensors (i.e., Silicon-PhotoMultipliers—SiPMs, Avalanche PhotoDiodes—APDs, etc.), displayed along the four sides of the gas gap; a uniform electric field between the two parallel electrodes to generate the gas avalanche multiplication. The scintillation light, produced during the avalanche processes, is read out by the array of collimated photosensors. The position of the avalanche is then computed as the center of gravity of the light recorded by the arrays of photosensors (Fig. 11).

The type and pressure of scintillating gas mixture that fills the detector may be determined by a number of factors, including type of application and experimental conditions, low operating voltages, high charge or scintillation yields, high rate capabilities, emission spectra that need to match

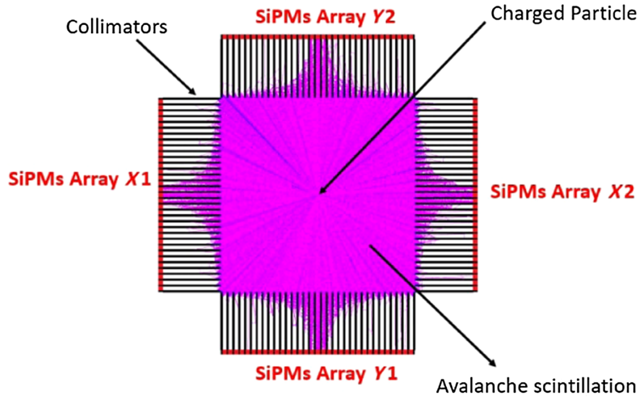

FIG. 11. Conceptual design of a PPAC with optical readout. Particle localization is accomplished by calculating the center of gravity of light collected by the photosensor arrays.

the properties of the photosensors, and short decay time that may offer good time resolution. Noble gases such as argon (Ar) and xenon (Xe) are highly efficient scintillating gases. However, since noble gases generally emit at very short wavelengths [47], solid-state photosensors would require wavelength shifters [e.g., TetraPhenyl Butadiene (TPB)] to ensure adequate photon detection. It is possible to obtain high scintillation yields from noble gases with a small amount of impurities, characterized by a lower excitation potential, so they can shift the wavelength to a more suitable visible range. However, pure noble gases and their mixtures, at low pressure, do not allow stable high-gain operation in open geometry configurations, due to intense photo-mediated secondary effects [22].

A unique combination of physical properties makes tetrafluoromethane gas (CF_4) a highly effective electro-luminesce medium: it is a heavy molecule consisting of light atoms, therefore it has high stopping power and low gamma sensitivity; it has a high electron drift velocity and low diffusion coefficient; it has good quenching properties, providing stable gas gain even at relatively low pressure (<10 Torr); it has a short scintillation decay time, with at least 90% of the light being emitted within about a few tens of nanoseconds.

A first one-dimensional optical PPAC (OPPAC) detector prototype has been developed and tested for the first time with heavy-ion beams, by the authors of this manuscript. A preliminary evaluation of the optical readout concept has been reported in [48]. Following this experience, an advanced two-dimensional prototype was constructed, equipped with optical readouts consisting of 4 arrays of 25 SiPMs mounted on a collimated frame, on each side of the PPAC volume. Figure 12 shows a photograph of the two-dimensional OPPAC prototype and an image of a calibration mask (the same as the one shown in Figs. 9 and 10). The image was obtained by irradiating uniformly the detector area with 5.9 MeV α particles. The detector achieved about 1 mm position resolution with only 25 SiPMs per array over the 100 mm long gas gap. Signals from individual SiPMs were processed and stored using a data acquisition system based on the General Electronics for TPCs (GET) [49].

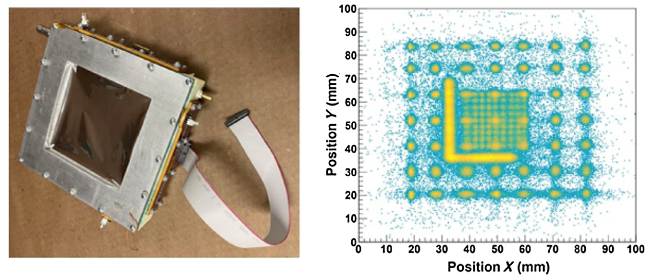

FIG. 12. Photograph of the two-dimensional OPPAC prototype (on the left side) and an image of a calibration mask obtained by irradiating the detector with 5.9 MeV α particles (on the right side).

A number of important features distinguish optical systems from conventional gas-avalanche detectors based on electron-ion readouts: faster pulse propagation, allowing for better time resolution; insensitivity to electronic noise and rf pickup problems since the readout is electrically decoupled from the active volume; a large light yield and a high granularity photon detector sensitive to single photo-electrons, which provide excellent energy signal-to-noise signals for a large dynamic range.

One of the disadvantages of optical readout methods is the requirement for a high-granularity data acquisition system, which increases the cost and complexity of the device. Additionally, the large amount of data that needs to be processed may limit the rate capability of the full tracking system.

VI. PPACS FOR HEAVY-ION BEAM TRACKING AT FRIB

The mechanical design, operational conditions, and performance optimization of the PPAC detectors currently in operation at FRIB are based on the solid experience matured in running the National Superconducting Cyclotron Laboratory (NSCL) over several decades, including the A1900 fragment separator [50]. The tracking system at NSCL was based on resistive-chain PPAC design [9], which ensured high detection efficiency and large dynamic range under a wide variety of experimental conditions. As discussed in previous sections, this readout scheme has the disadvantage of having an extremely low rate capability, which cannot exceed a few kHz at best. Despite this, the main purpose of the tracking system at the A1900 fragment separator was to facilitate tuning and delivery of beams prior to any experimental run. The task was achieved by providing the necessary characterization of beam properties, including measurements of two-dimensional beam profiles, trajectory angles, and transmission through the A1900 beam line.

In the wake of FRIB operations, diagnostics and tracking system functionalities and requirements for the fragment separator were redefined. FRIB includes a superconducting driver accelerator and the Advanced Rare Isotope Separator (ARIS) [51]. The driver linac is designed to accelerate all stable ions above 200 MeV/u with 400 kW beam power [52]. It is expected that FRIB will enable access to more than 1000 new isotopes and provide beams at much larger rates compared to NSCL. ARIS provides in-flight separation of projectile fragments and transports the rare isotope fragments of interest to serve a wide experimental science program. It consists of a vertical preseparator and a horizontal separator section (C-bend) and supports various operational modes, including momentum compression using a wedge shape degrader.

At FRIB, delay-line readout PPACs (DLPPACs) were developed and constructed to replace the old resistive-chain architecture and meet the more demanding rate capability requirements. With the implementation of DLPPACs, the tracking system in ARIS could be improved by 2 orders of magnitude in rate [53]. In addition, DLPPAC fast timing signals can be used in conjunction with plastic scintillators for improving time-of-flight measurement accuracy. In general, a time resolution of a few hundred psec can be achieved, which is comparable to that of small-area plastic scintillator detectors. Timing measurements provided by DLPPACs alone were also suggested for high beam rates (approaching 1 MHz) over extended periods of time, as plastic scintillator material does not sustain large radiation doses.

In this regard, some aging problems have also been observed in DLPPAC, in the form of a degradation of the cathode conductivity due to the bombardments of an intense flux of avalanche cations. With the impact of ions on the electrode, the metal surface gradually evaporates and the detection efficiency of the device slowly decreases. The DLPPACs, however, are more robust than plastic scintillators. Under the same conditions of absorbed dose, the degradation of DLPPAC performance is generally slower than that of plastic scintillators.

In ARIS, DLPPACs are installed at various locations, from the production target area (wedge station of the preseparator) to the last focal-plane diagnostics station (DB5) of the fragment separator—see Fig. 13. In order to accommodate a variety of operational modes and beam optics characteristics, detectors with different effective areas have been designed and fabricated. The wedge area contains two DLPPCs with an area of $30 \times 5\ \mathrm{cm}^2$ used for beam diagnostic purposes, beam transmission studies, and correction of high-order aberrations. The two focal planes, DB1 and DB5, at the extreme ends of the horizontal section of the fragment separator contain a couple of $10 \times 10\ \mathrm{cm}^2$ DLPPACs separated by 0.4 m, intended for position measurement with about 0.5 mm resolution such that transverse angles for each particle can be evaluated. In between the two external focal planes, a couple of DLPPAC of area $20 \times 10\ \mathrm{cm}^2$ and a single DLPPAC of area $20 \times 5\ \mathrm{cm}^2$ are installed in DB3 and DB4, respectively. The single DLPPAC at DB4 can be used to determine particle momentum given the large 15.4 mm% dispersion at that location [54].

The following section provides some technical details regarding the construction and operation of DLPPAC detectors as a tracking system and beam diagnostic tool at the ARIS fragment separation, including a description of fabrication, choice of materials, and an overview of the detector performance.

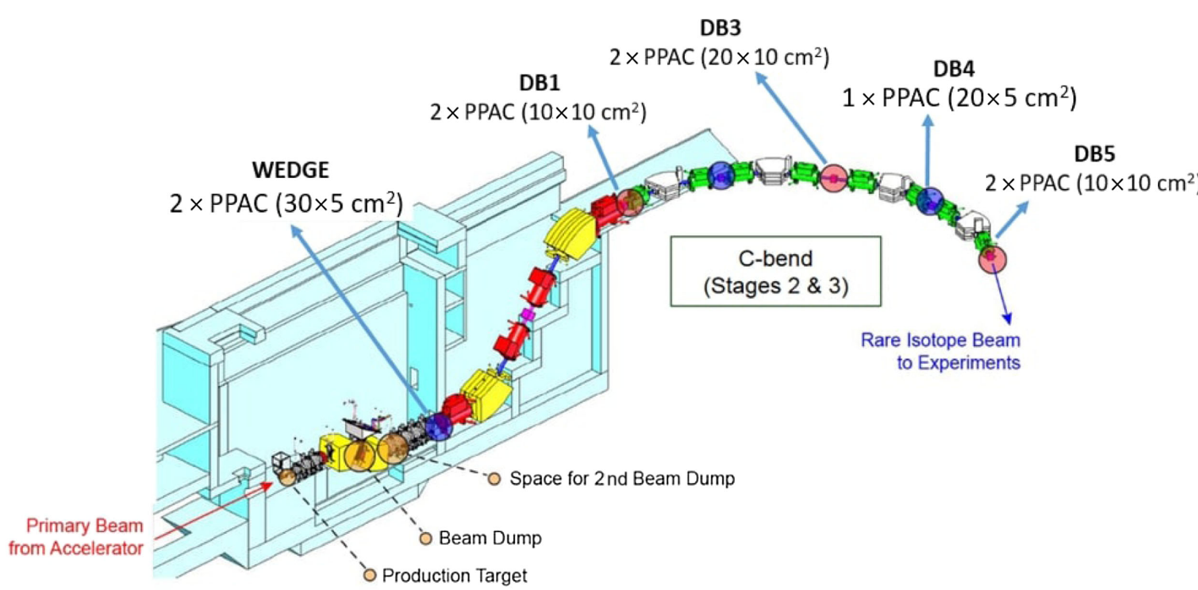

FIG. 13. Overview of the design of the Advanced Rare Isotope Separator (ARIS) at FRIB.

A. FRIB DLPPAC design and construction

A FRIB DLPPAC detector consists of a single uniform cathode foil, common to both (X,Y) counters, sandwiched between two striped anode foils. All the electrodes are glued on the surfaces of PCB_1 and PCB_2 (see Fig. 14), using rubber cement. The cathode foil is kept between the two PCBs (PCB_1 and PCB_2), while the anode foils are fastened to the opposite surfaces. The PCBs serve as support for the foils and define the gas gap in the DLPPAC counters (equal to 3.5 mm). In addition, the PCBs host the traces for the bias of the cathode, and the pads of the delay line electrically connected to the anode strips. Finally, the PCBs also host the first-stage preamplifiers used to process the signals from the cathode (which provides time measurement and trigger) and from the delay line (for position measurement). All the above DLPPAC components are assembled inside a vacuum-tight aluminum vessel, which also includes inlet and outlet gas fittings; a safe high voltage (SHV) panel-mount connector used to deliver the bias to the cathode electrode; a 26-pin insulation-displacement contact (IDC) connector for supplying the low-voltage power for the custom-made, fast-current preamplifiers and routing out the delay-line signals. The aluminum vessel is sealed on both sides by two pressure windows, made of metalized Mylar film glued to an aluminum frame. A Buna-N o-ring is interlaced between the pressure window frames and the body of the vessel in order to maintain a good vacuum level outside the PPAC (below 10^{-5} Torr). The DLPPAC pressure windows can withstand a maximum differential pressure of 25 Torr, whereas the DLPPACs are routinely operated at a maximum pressure of about 15 Torr.

The DLPPAC detectors in ARIS are filled with isobutane (C_4H_{10}) because of its excellent photon quenching properties at low pressures, which provides a more stable high gain operation than in other types of gases. The only exception is the wedge-station DLPPAC, in the preseparator area, loaded with nonflammable octafluoropropane (C_3F_8) for safety reasons. Detectors are evacuated at a vacuum level of 10^{-6} Torr prior to gas filling. During operation, the gas is continuously flowing at a rate of 4–5 sccm to remove impurities.

The signals from the four delay-line terminations and the anode electrodes are processed by a two-stage fast-current preamplifier. First-stage boards are installed directly on the inner PCBs, within the detector vessel and provide 20 dB gain with differential outputs. The input impedance of the first stage is designed to match the 100 Ω impedance of the delay line to avoid reflections along the conductive lines. In addition, the outputs are routed out of the detector vessel by a 26-pin IDC connector mounted on one of the pressure window frames. Figure 15 shows the interior of a $10 \times 10\ \mathrm{cm}^2$ DLPPAC vessel. The second-stage preamplifiers are kept in air outside the diagnostics box and are connected to the first stage by a flat cable via a suitable flange feedthrough. The second stage provides an additional 10 dB of gain, with single-ended output terminated at 50 Ω. Both the first stage and second stage boards are equipped with a first-order low pass filter with a −3 dB cutoff at about 25 MHz.

The anode and cathode electrodes are made from polypropylene foils with a thickness of 0.75 μm. They are fabricated using an apparatus similar to that designed by Barrus and Blake [55]. A thickness of 15 μg/cm has been demonstrated with this technique, and the homogeneity and strength are excellent.

An electron gun evaporator process is used to metalize the foils (150 nm thick layer) after they have been stretched onto aluminum frames. Gold, aluminum, and recently chromium are the most common metal coating substances. Aluminum evaporates easily because of its low melting point and it is also affordable. However, it oxidizes in contact with air and is less stable than gold. The latter ensures long-term stability, but it is expensive. When it comes to spark resistance, chromium is an excellent alternative: its high melting point (1.9k °C compared to

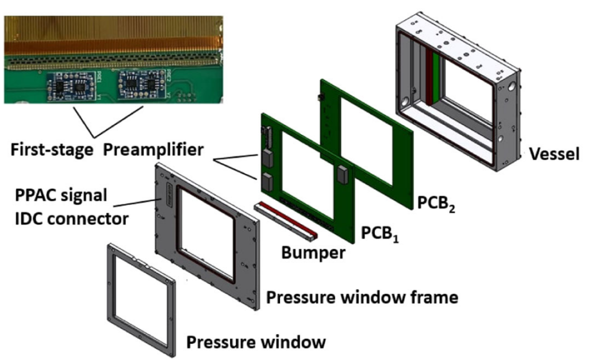

FIG. 14. Exploded view of the mechanical model of a $10 \times 10\ \mathrm{cm}^2$ FRIB DLPPAC. The top portion of the figure shows a photograph of the delay line and miniaturized fast-current preamplifiers used to process the delay-line signals.

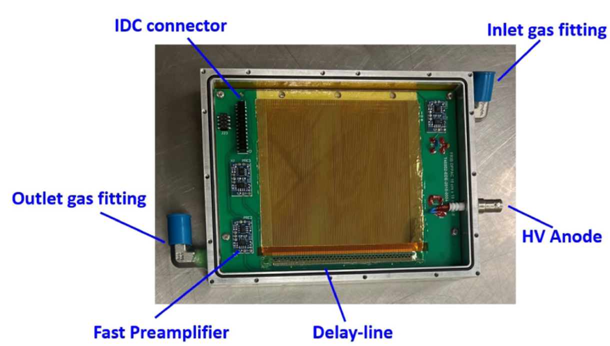

FIG. 15. Photograph of the interior of a $10 \times 10\ \mathrm{cm}^2$ DLPPAC vessel. Four screws are used to fasten the PCB that supports the segmented anode electrodes and the cathode to the vessel's corners. The PCBs also host fast-current preamplifiers. The vessel is equipped with proper interfaces for gas flow and anode voltage bias.

1k °C of gold) should enable it to withstand and better dissipate the energy released during the discharges, thus preventing localized evaporation of the thin metal layer. Single-side striped anode foils are fabricated by placing a striped mask in front of the electrode foil during evaporation. The pitch between strips is 1.27 mm (0.05 inch), with dead space between the strip of 0.254 mm (0.01 inch). The cathode foil is uniformly evaporated on both sides.

The electrodes are then fastened onto the PCB boards by aligning the anode strips to the delay-line pads. The electrical connection between the anode strips and the pads is maintained by pressing the foil on the PCB with a bumper installed on the pressure window frame.

Approximately, 25 complete devices have been constructed and are used in ARIS and on the beam line of the S800 spectrometer. Other DLPPACs are planned for future infrastructure (the high rigidity spectrometer [56] and the Sweeper magnet [57]). Circuit boards of equal effective areas are interchangeable, allowing for the maintenance of a reasonable inventory of components and the assembly of replacement detectors in a timely manner. Except for the foils, the components are extremely durable, and mechanical failures are rare (<1%), even after numerous disassemblies involving extensive cleaning and handling. However, after extensive use, the contact between the delay-line taps and the stripes on the readout foils degrades, reducing signal strength. The inner PCBs are regularly refurbished to avoid loss of response.

B. Design of the delay line

The design of the passive delay-line circuitry for the FRIB DLPPAC complies with the general guidelines described in Sec. V B. For all detector sizes, the total delay line along a coordinate is approximately 10 nsec/cm. As the time resolution of the data acquisition (DAQ) system, based on a Mesytec constant fraction discriminator, and a Mesytec time-to-digital converter (MTDC-32), was configured to be 0.1 nsec, the lowest achievable spatial resolution is about 0.1 mm.

To prevent signal attenuation along the coordinates, the selection of inductors with a minimum dc resistance (R_{dc}) is an important parameter in the design of delay-line circuitry. The output voltage attenuation of a delay line is expressed as

$$\mathrm{Attenuation} = 1 - \frac{Z_0}{Z_0 + R_{DC}}, \tag{24}$$

where Z_0 is the total impedance of the delay line. As an example, in the case of a $10 \times 10\ \mathrm{cm}^2$ DLPPAC, the selected inductors had a nominal dc resistance of about 0.1 mΩ, which corresponds to a total dc resistance of approximately 7–8 Ω along the full delay line. This corresponds to a signal voltage attenuation across the entire delay line of only about 8%.

The passive delay line was properly integrated into the circuit design to ensure delay accuracy and prevent signal distortion. In particular, we added a massive ground plane on the PCBs and minimized trace lengths to the delay-line terminations to avoid loading a tap with several picofarads of capacitance, which could increase delay, rise time, distortion, and attenuation. The fast-current preamplifier inputs were grounded to a common ground plane to avoid ground loop issues.

C. DLPPAC performance

Prior to commissioning at FRIB, all DLPPACs undergo benchmark tests to verify their operation and performance. The stability of the gas gain and the quality of the two-dimensional images are determined by irradiating the detectors with a few MeV α particles from a small-rate source (either Am-241 or Th-228). The DLPPACs are installed in a large vacuum chamber equipped with a dedicated gas handling system and a DAQ for signal processing and data storage. In accordance with best practices, before filling the detectors, the vacuum chamber and the DLPPACs are simultaneously evacuated at a vacuum level of 10^{-5} Torr to remove any residual impurities (oxygen and outgassing from the detector components). The DLPPACs are then filled with isobutane at a constant pressure within the 7–13 Torr range.

At a pressure of 7 Torr, the central electrode foil of the DLPPACs is normally biased with approximately −700 V. This produces signals from the preamplifier outputs on the order of a few hundred mV for the fast electron component. Signals have 10–15 nsec rise time.

The results of a typical position calibration of a $10 \times 10\ \mathrm{cm}^2$ DLPPPAC can be seen in Fig. 16 (right side). The image was recorded by irradiating a brass mask (see left side of Fig. 16) placed in front of the device. The small holes in the central region of the mask have a diameter of 1 mm and a pitch of 2.5 mm and are clearly resolved in the DLPPAC image. Based on the assumption that the hole diameter contributes 2/3 to the measured holes' images (equals to the ratio of the distance pinhole-to-detector to the distance source-to-pinhole), the intrinsic resolution results to be approximately 0.5 mm (FWHM). An equivalent estimate of the detector's position resolution is made using edge-spread function analysis. In this case, the detector's position resolution is defined as the FWHM of the derivative (point spread function) of the L-shaped edge profile (edge spread function) seen in the center of the image in Fig. 17. As the intrinsic resolution of the delay line is better than the pitch (1.27 mm) between strips of the anode readout, the projection of the L-shape mask aperture shows a rough pixelization. The two peaks on the profile graph of Fig. 17 correspond to two strips located within the L-shape aperture of the mask. In spite of some low statistics, the edge spread function analysis estimates a

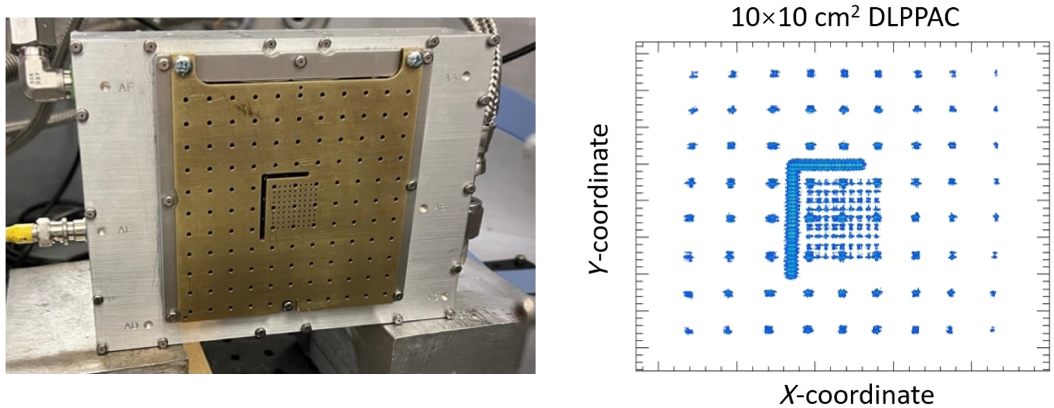

FIG. 16. Arrangement for the test for the DLPPAC performance evaluation (left) and image of the pinholes brass mask (right), obtained by irradiating the detector with 5.9 MeV α particles.

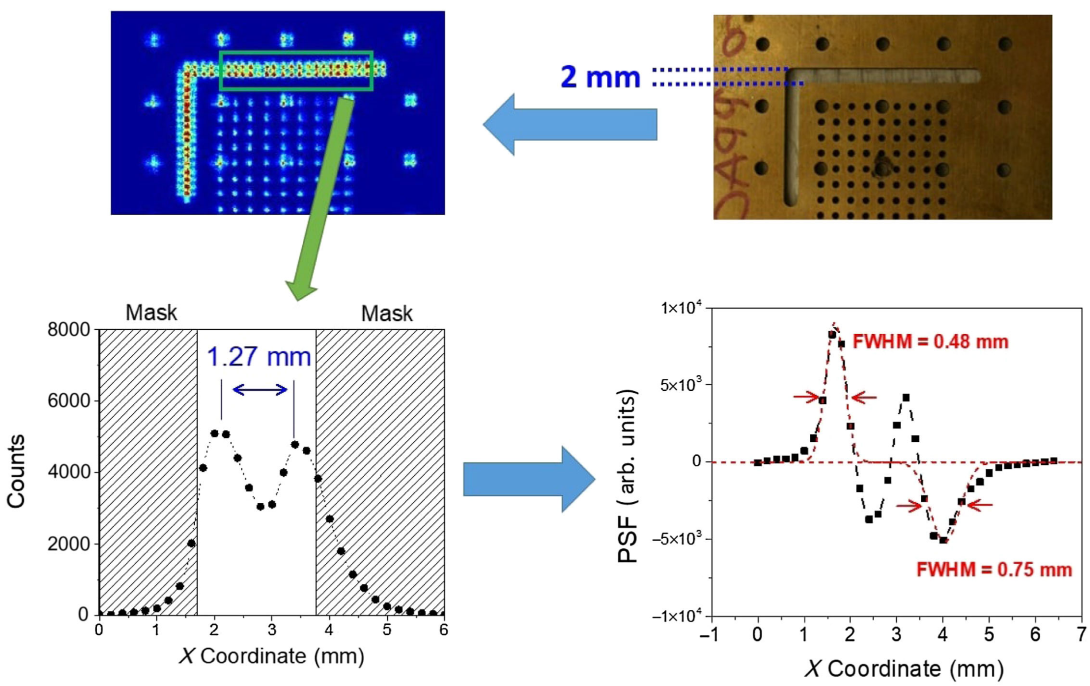

FIG. 17. Edge spread function analysis of the calibration mask image for the estimation of the position resolution achieved by a 10×10 cm^2 DLPPAC. As a result of the intrinsic resolution of the system being better than delay-line space segmentation (1.27 mm pitch), the image is subdivided into many points corresponding to the intersection between the *x* coordinate strips and the *y* coordinated strips.

position resolution of approximately 0.5–0.75 mm (FWHM), in line with our previous estimation.

The detector is capable of providing images with excellent linearity, and the detection efficiency is uniform throughout the entire effective area. Figure 18 illustrates an example of an image obtained with the detector effective area fully exposed to the α-particle source (empty field image). Because the source was located at a relatively close distance to the DLPPAC entrance windows, the central region of the detector's effective area recorded a greater number of events than the perimeter. The histogram of the total number of recorded counts per pixel is thus affected by a high variance, but the overall image appears rather homogeneous, and the detection efficiency is uniform. A good linearity has also been observed (Fig. 19), with an estimated integral nonlinearity of only about 0.26%.

As discussed in Sec. II A, DLPPACs provide excellent time resolution. Figure 20 (top diagram) illustrates the arrangement used to evaluate the timing properties of the DLPPACs installed at the C-bend portion of ARIS. The measurement was performed with the 20×10 cm^2 DLPPACs installed on the intermediate diagnostic station

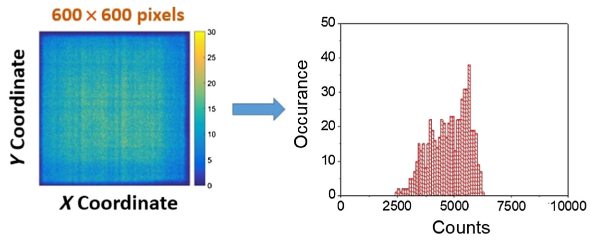

FIG. 18. Histogram analysis (on the right) of an empty field image (on the left) for evaluating the uniformity of the detector response throughout the entire effective area.

(DB3) and compared to the response of a small plastic scintillator read out by a photomultiplier tube, located at the first focal plane (DB1). For both time-of-flight measurements, the time reference was provided by a silicon PIN diode (Micron Semiconductor model MSX25), located at the end of the C-bend section (DB5). The detectors were irradiated with a beam of ^{106}Sn ions, at an energy of about 200 MeV/u. The beam rate was about 1 kHz.

In the optimal operating conditions of relatively low voltage biases, both DLPPACs achieve a time resolution of 250 psec (Fig. 20, bottom left). This timing performance is comparable to that of the plastic scintillator-based detector (about 200 psec), but with the advantage of less anticipated aging degradation. Contrary to our expectation, the time resolution noticeably degraded at higher gains (for voltage bias above 600 V in Fig. 20, bottom right). With an increase in detector gain, the probability of sporadic discharges increases proportionally, affecting the stability of the detector significantly. More frequent sparks induce an increase in detector dead time, as well as a longer recovery time during which the optimal timing response of the device is temporarily compromised. Nevertheless, there is a wide range of operational conditions for which good time resolution and full efficiency are achieved, within a relatively large dynamic range. It should be noted that the results discussed above and shown in Fig. 20 include the contribution of a PIN diode detector coupled with a charge-sensitive preamplifier, a combination notoriously known for its slow response time. As a result, the actual intrinsic time resolution of the DLPPAC, as well as the plastic scintillator, is expected to be better than the one reported here. Moreover, two additional factors contribute greatly to the difference in measured time resolution between the DLPPAC and the plastic scintillator: the momentum spread of the beam and the different flight paths. Upon removing these two additional contributions, the DLPPAC intrinsic time resolution is expected to be better than 100 psec.

The beam optics of the ARIS fragment separator was designed to have certain transverse phase space at each focal point to separate the fragments [51]. The tuning of quadrupoles is required in order to match the beam transversely during operation. Before tuning, DLPPAC-based tracking is used to measure the transverse phase space. Beam divergence angles (x' and y') can be calculated based on the difference in position and time between the two DLPPACs of a focal point. Figure 21 shows an example of the phase-space plots along the X and Y planes obtained from the DLPPACs at DB1 (Fig. 13) for a ^{64}Fe beam, after transverse matching has been performed [58].

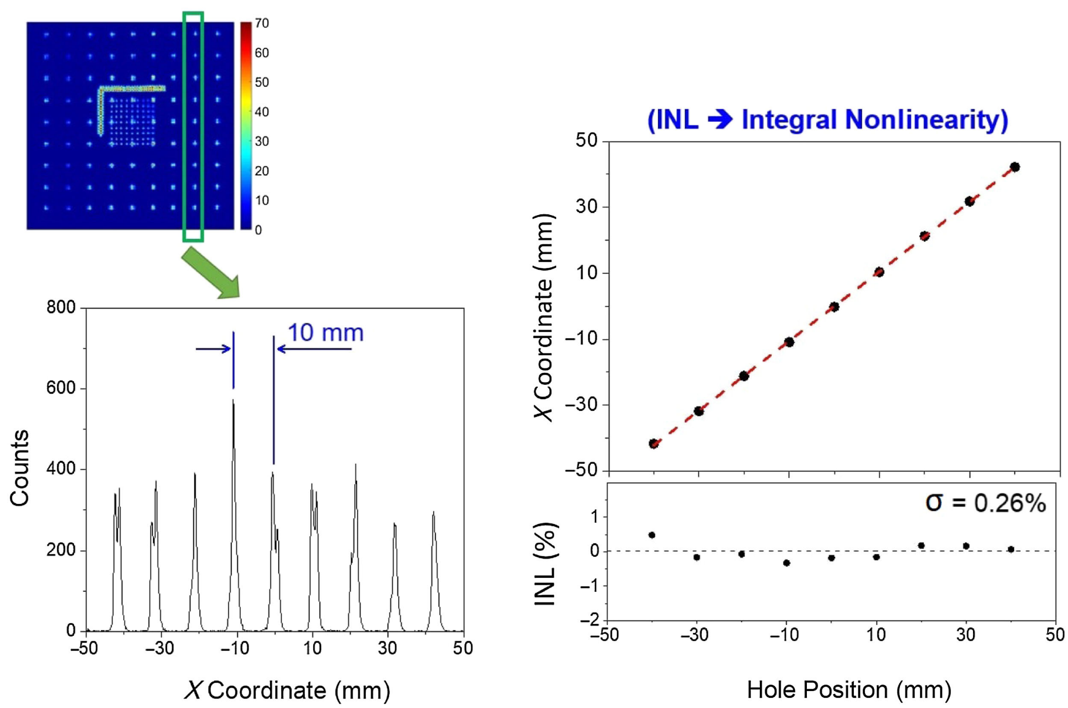

FIG. 19. Integral nonlinearity (INL) analysis of the calibration mask image—variation of the INL is below 0.3%.

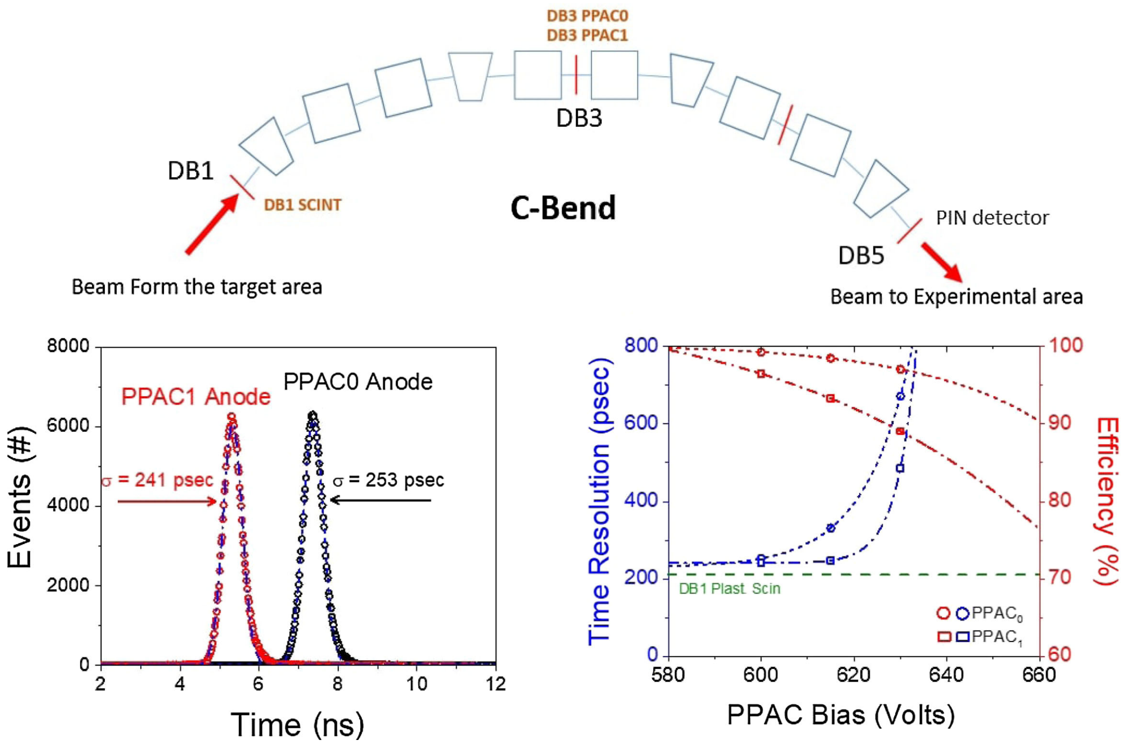

FIG. 20. Setup for the timing performance evaluation of the DLPPAC (top diagram). The measured time resolution provided by the DLPPAC is about 250 psec (bottom left graph). Results of time resolution and detection efficiency are also shown on the bottom right graph.

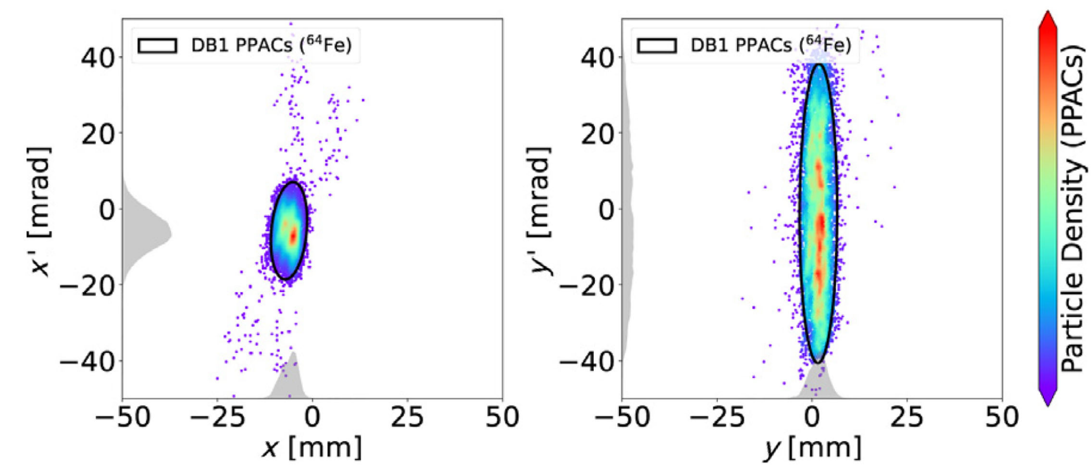

FIG. 21. Transverse phase space of ^{64}Fe fragment beam measured by DLPPACs installed in diagnostics station DB1, after transverse matching. The left figure shows the horizontal phase space and the right figure shows the vertical phase space. Graph taken from [58].

The ellipses drawn on each phase space plot represent the emittance boundaries in the first order approach using the root mean square and covariance values [54].

VII. SUMMARY AND CONCLUSION

This paper presents and discusses the principles of operation, design, and specifications, types of readout methods, and performance of the PPAC detector technology.

PPACs are simple devices, inexpensive, and easy to maintain. Submillimeter spatial resolutions (FWHM) can be realized with a segmented (strip) readout, even with a coarse center-to-center (pitch) strip separation of above 1 mm. The counting rate capability of conventional PPACs with charge-division readout methods is limited to a few tens of kHz, while delay-line PPACs can reach up to 1 MHz for extended beam sizes, before encountering loss of detection efficiency and instabilities.

Despite being an old detector technology, PPACs are still a valuable tool in heavy-ion beam physics and continue to be the best solution for measuring the ion's trajectory to determine the magnetic rigidity (Bρ) with high precision for particle identification purposes. Beam diagnostics and fine beam tuning are carried out with PPACs at the major isotope beam facilities throughout the world.

We have described the current design and performance of the delay-line PPACs in operation at FRIB, including a detailed overview of the problems and possible alternatives for future developments.

ACKNOWLEDGMENTS

Work supported by the U.S. Department of Energy Office of Science under Cooperative Agreement No. DE-SC0023633, the State of Michigan, and Michigan State University. This manuscript was prepared with the support, encouragement, and suggestions provided by the FRIB members of the radiation detector lab, Beam Measurements and Instrumentation department (BIM), and the ARIS beam physicist group. The authors would also like to thank Sean Dziubinski for the meticulous revision of the text.

[1] J. Christiansen, Self-quenching parallel-plate vapor counter at voltages below the static breakdown field strength, Z. Angew. Phys. **4**, 326 (1952), https://www.osti.gov/biblio/4392815.

[2] J. Christiansen, G. Hempel, H. Ingwersen, W. Klinger, G. Schatz, and W. Witthuhn, Investigation of delayed fission in 236 U, Nucl. Phys. **A239**, 253 (1975).

[3] H. Stelzer, A large area parallel plate avalanche counter, Nucl. Instrum. Methods **133**, 409 (1976).

[4] W. Seidel, H.-G. Ortlepp, F. Stary, and H. Sodan, Double-grid avalanche counter with large dynamic range, Nucl. Instrum. Methods Phys. Res., Sect. A **273**, 536 (1988).

[5] J. Cub, C. Gund, D. Pansegrau, G. Schrieder, and H. Stelzer, A position sensitive parallel plate avalanche counter for single particle and current readout, Nucl. Instrum. Methods Phys. Res., Sect. A **453**, 522 (2000).

[6] A. Manna *et al.* (n_TOF Collaboration), Recoil proton telescopes and parallel plate avalanche counters for the $^{235}\mathrm{U(n,f)}$ cross section measurement relative to H(n,n)H between 10 and 450 MeV neutron energy, J. Instrum. **18**, P04024 (2023).

[7] H. Kumagai, T. Ohnishi, N. Fukuda, H. Takeda, D. Kameda, N. Inabe, K. Yoshida, and T. Kubo, Development of Parallel Plate Avalanche Counter (PPAC) for BigRIPS fragment separator, Nucl. Instrum. Methods Phys. Res., Sect. B **317**, 717 (2013).

[8] C. Akers, K. B. Lee, Y. J. Kim, T. Hashimoto, E. H. Kim, H. S. Lee, J. H. Park, M. S. Ryu, K. Tshoo, B. H. Kang, and Y. K. Kwon, Large area PPAC development at the rare isotope science project, Nucl. Instrum. Methods Phys. Res., Sect. A **910**, 49 (2018).

[9] D. Swan, J. Yurkon, and D. Morrissey, A simple two-dimensional PPAC, Nucl. Instrum. Methods Phys. Res., Sect. A **348**, 314 (1994).

[10] W. Shockley, Currents to conductors induced by a moving point charge, J. Appl. Phys. **9**, 635 (1938).

[11] S. Ramo, Currents induced by electron motion, Proc. IRE **27**, 584 (1939).

[12] H. Raether, *Electron Avalanches and Breakdown in Gases*, Butterworths Advanced Physics Series (Butterworths, London, 1964).

[13] John S. Townsend and P. J. Kirkby, LXIII. Conductivity produced in hydrogen and carbonic acid gas by the motion of negatively charged ions, Philos. Mag. **1**, 630 (1901).

[14] J. Townsend, XXXVIII. The conductivity produced in gases by the aid of ultra-violet light, Philos. Mag. **5**, 389 (1903).

[15] J. Townsend, LXXVI. The genesis of ions by the motion of positive ions in a gas, and a theory of the sparking potential, Philos. Mag. **6**, 598 (1903).

[16] E. Nappi and V. Peskov, *Imaging Gaseous Detectors and Their Applications* (Wiley, New York, 2013).

[17] Y. Giomataris, P. Rebourgeard, J. P. Robert, and G. Charpak, MICROMEGAS: A high granularity position sensitive gaseous detector for high particle flux environments, Nucl. Instrum. Methods Phys. Res., Sect. A **376**, 29 (1996).

[18] R. M. Corless, G. H. Gonnet, D. E. G. Hare, D. J. Jeffrey, and D. E. Knuth, On the LambertW function, Adv. Comput. Math. **5**, 329 (1996).

[19] Y. I. Davydov, On the first Townsend coefficient at high electric field, IEEE Trans. Nucl. Sci. **53**, 2931 (2006).

[20] F. Sauli, *Gaseous Radiation Detectors: Fundamentals and Applications* (Oxford University Press, New York, 2015), Vol. 36.

[21] G. Charpak, Evolution of the automatic spark chambers, Annu. Rev. Nucl. Sci. **20**, 195 (1970).

[22] P. Fonte, V. Peskov, and F. Sauli, Feedback and breakdown in parallel plate chambers, Nucl. Instrum. Methods Phys. Res., Sect. A **305**, 91 (1991).

[23] Y. Fu, P. Zhang, J. P. Verboncoeur, and X. Wang, Electrical breakdown from macro to micro/nano scales: A tutorial and a review of the state of the art, Plasma Res. Express **2**, 013001 (2020).

[24] O. Sahin, I. Tapan, and R. Veenhof, Secondary avalanches in gas mixtures, Nucl. Instrum. Methods Phys. Res., Sect. A **718**, 432 (2013).

[25] L. E. Kline and J. G. Siambis, Computer simulation of electrical breakdown in gases; avalanche and streamer formation, Phys. Rev. A **5**, 794 (1972).

[26] T. G. Klämpfl, Cold atmospheric plasma decontamination against nosocomial bacteria, Ph.D. thesis, Technische Universität München, 2014.

[27] J. M. Meek, A theory of spark discharge, Phys. Rev. **57**, 722 (1940).

[28] V. Peskov and P. Fonte, Research on discharges in micro-pattern and small gap gaseous detectors, arXiv:0911.0463.

[29] F. Sauli, Micro-pattern gas detectors, Nucl. Instrum. Methods Phys. Res., Sect. A **477**, 1 (2002).

[30] C. Akers, K. B. Lee, Y. J. Kim, E. H. Kim, Y. K. Kwon, H. S. Lee, J. Y. Moon, J. H. Park, M. S. Ryu, T. Shin, and

S. Yoshiteru, Construction and performance test of prototype parallel plate avalanche counters at RAON, J. Korean Phys. Soc. **70**, 682 (2017).

[31] X. Wei *et al.*, Development of parallel plate avalanche counter for heavy ion collision in radioactive ion beam, Nucl. Eng. Tech. **52**, 575 (2020).

[32] S. Yang, C. Luo, H. Lin, P.-P. Xu, L. Xu, J. Lei, G.-J. Zhong, and Z.-M. Li, Robust propylene-ethylene copolymer/polypropylene films: Extensional stress-induced orientation realized at low temperature processing, Polymer **206**, 122848 (2020).

[33] D. Lee, C. Akers, M. Kwag, K. B. Lee, H. Park, and K. Tshoo, Fabrication and performance evaluation of parallel plate avalanche counters for RISP, Nucl. Instrum. Methods Phys. Res., Sect. A **1014**, 165734 (2021).

[34] S. Hanai, S. Ota, R. Kojima, S. Masuoka, M. Dozono, N. Imai, S. Michimasa, S. Shimoura, J. Zenihiro, K. Inaba, and Y. Hijikata, Development of strip-readout PPAC for high-intensity heavy ions, Nucl. Instrum. Methods Phys. Res., Sect. B **541**, 194 (2023).

[35] E. Norbeck, J. E. Olson, and Y. Onel, A new look at the PPAC, Acta Phys. Hung. A **25**, 469 (2006).

[36] M. Cortesi, Y. Ayyada, and J. Yurkon, Development of a Parallel-Plate avalanche counter with optical readout (O-PPAC), J. Instrum. **13**, P10006 (2018).

[37] T. Kubo, M. Ishihara, N. Inabe, H. Kumagai, I. Tanihata, K. Yoshida, T. Nakamura, H. Okuno, S. Shimoura, and K. Asahi, The RIKEN radioactive beam facility, Nucl. Instrum. Methods Phys. Res., Sect. B **70**, 309 (1992).

[38] L. Lindgren and A. Sandell, An investigation of two position-sensitive PPACS, Nucl. Instrum. Methods Phys. Res. **219**, 149 (1984).

[39] R. Bellazzini, A. Del Guerra, M. Massai, M. Ragadini, G. Spandre, and G. Tonelli, A MWPC with a cathode coupled delay line read-out as radioactivity detector for dna repair studies, Nucl. Instrum. Methods Phys. Res. **190**, 627 (1981).

[40] W. Bertozzi, M. Hynes, C. Sargent, C. Creswell, P. Dunn, A. Hirsch, M. Leitch, B. Norum, F. Rad, and T. Sasanuma, Focal plane instrumentation: A very high resolution MWPC system for inclined tracks, Nucl. Instrum. Methods **141**, 457 (1977).

[41] J. Lopez-Robles, R. Alfaro, E. Belmont-Moreno, V. Grabski, A. Martinez-Davalos, and A. Menchaca-Rocha, Improving MWPC delay line readout by waveform analysis, IEEE Trans. Nucl. Sci. **52**, 2841 (2005).

[42] A. Breskin, R. Alon, M. Cortesi, R. Chechik, J. Miyamoto, V. Dangendorf, J. Maia, and J. Dos Santos, A concise review on THGEM detectors, Nucl. Instrum. Methods Phys. Res., Sect. A **598**, 107 (2009).

[43] M. Cortesi, R. Chechik, A. Breskin, G. Guedes, V. Dangendorf, D. Vartzky, and D. Bar, Advances in imaging THGEM-based detectors, Nucl. Instrum. Methods Phys. Res., Sect. A **572**, 175 (2007).

[44] Z. Korkulu, L. Stuhl, S. Naimi, Z. Dombrádi, K. Hahn, J. Moon, D. Ahn, Z. Halász, and G. Hudson-Chang, A position-sensitive large-area microchannel plate detector with digital data-acquisition system for studies of exotic nuclei, Nucl. Instrum. Methods Phys. Res., Sect. B **541**, 232 (2023).

[45] T. Liu, Z. Xu, R. Mao, Y. Yuan, Z. Yao, L. Yao, J. Hu, J. Li, Y. Feng, J. Ding, and F. Liu, Design and performance of micro-channel plate based particle tracking detector for astrophysical (alpha, p) reactions, Nucl. Instrum. Methods Phys. Res., Sect. A **959**, 163599 (2020).

[46] M. Cortesi, A. Stolz, and J. Yurkon, Measurements of secondary scintillation in low-pressure CF4 with a SiPM, from a parallel-plate avalanche geometry, J. Instrum. **11**, P04017 (2016).

[47] R. Henck and A. Coche, Studies on noble gas scintillators, IEEE Trans. Nucl. Sci. **14**, 478 (1967).

[48] M. Cortesi, Y. Ayyad, and J. Yurkon, Development of a parallel-plate avalanche counter with optical readout (O-PPAC), J. Instrum. **13**, P10006 (2018).

[49] E. Pollacco *et al.*, GET: A generic electronics system for TPCs and nuclear physics instrumentation, Nucl. Instrum. Methods Phys. Res., Sect. A **887**, 81 (2018).

[50] D. Morrissey, B. Sherrill, M. Steiner, A. Stolz, and I. Wiedenhoever, Commissioning the a1900 projectile fragment separator, Nucl. Instrum. Methods Phys. Res., Sect. B **204**, 90 (2003).

[51] M. Hausmann, A. Aaron, A. Amthor, M. Avilov, L. Bandura, R. Bennett, G. Bollen, T. Borden, T. Burgess, S. Chouhan, V. Graves, W. Mittig, D. Morrissey, F. Pellemoine, M. Portillo, R. Ronningen, M. Schein, B. Sherrill, and A. Zeller, Design of the advanced rare isotope separator ARIS at FRIB, Nucl. Instrum. Methods Phys. Res., Sect. B **317**, 349 (2013).

[52] J. Wei *et al.*, Accelerator commissioning and rare isotope identification at the facility for rare isotope beams, Mod. Phys. Lett. A **37**, 2230006 (2022).

[53] J. Wei *et al.*, Technological developments and accelerator improvements for the FRIB beam power ramp-up, J. Instrum. (to be published).

[54] M. Portillo, B. Sherrill, Y. Choi, M. Cortesi, K. Fukushima, M. Hausmann, E. Kwan, S. Lidia, P. Ostroumov, R. Ringle, M. Smith, M. Steiner, O. Tarasov, A. Villari, and T. Zhang, Commissioning of the advanced rare isotope separator ARIS at FRIB, Nucl. Instrum. Methods Phys. Res., Sect. B **540**, 151 (2023).

[55] D. M. Barrus and R. L. Blake, Technique for producing ultrathin polypropylene films, Rev. Sci. Instrum. **48**, 116 (1977).

[56] S. Noji, R. Zegers, G. Berg, A. Amthor, T. Baumann, D. Bazin, E. Burkhardt, M. Cortesi, J. DeKamp, M. Hausmann, M. Portillo, D. Potterveld, B. Sherrill, A. Stolz, O. Tarasov, and R. York, Design of the high rigidity spectrometer at FRIB, Nucl. Instrum. Methods Phys. Res., Sect. A **1045**, 167548 (2023).

[57] J. Toth, M. Bird, J. Miller, S. Prestemon, J. DeKamp, L. Morris, M. Thoennessen, and A. Zeller, Final design of a compact sweeper magnet for nuclear physics, IEEE Trans. Appl. Supercond. **12**, 341 (2002).

[58] K. Fukushima, M. Cortesi, M. Hausmann, E. Kwan, P. Ostroumov, M. Portillo, B. Sherrill, M. Smith, M. Steiner, and T. Zhang, Simulation studies for beam commissioning at FRIB advanced rare isotope separator, Nucl. Instrum. Methods Phys. Res., Sect. B **541**, 53 (2023).